WAlSiN-based solar selective coating stability-study under heating and cooling cycles in vacuum up to 800 °C using in situ Rutherford backscattering spectrometry and spectroscopic ellipsometry

Niranjan, K.; Krause, M.; Lungwitz, F.; Munnik, F.; Hübner, R.; Pemmasani, S. P.; Escobar Galindo, R.; Barshilia, H. C.;

Originally published:

March 2023

Solar Energy Materials and Solar Cells 255(2023), 112305

DOI: https://doi.org/10.1016/j.solmat.2023.112305

WAlSiN-based solar selective coating stability-study under heating and cooling cycles in vacuum up to 800 °C using *in situ* Rutherford backscattering spectrometry and spectroscopic ellipsometry

K. Niranjan[1#], M. Krause[2#], F. Lungwitz[2], F. Munnik[2], R. Hübner[2], S. P. Pemmasani[1], R. Escobar Galindo[3], H. C. Barshilia[1*]

[1] *Nanomaterials Research Laboratory, Surface Engineering Division, CSIR-National Aerospace Laboratories, Bangalore, India*

[2] *Helmholtz-Zentrum Dresden – Rossendorf, Bautzner Landstraße 400, 01328 Dresden, Germany*

[3] *Departamento de Física Aplicada I, Escuela Politécnica Superior, Universidad de Sevilla, Virgen de África 7, 41011-Sevilla, Spain*

([#]K.N. and M.K. contributed to the manuscript to equal parts.)

Abstract

In situ Rutherford Backscattering Spectrometry (RBS) and Spectroscopic Ellipsometry (SE) were applied to study the compositional and optical stability of a WAlSiN-based solar-selective coating (SSC) at high temperatures in vacuum. The samples were exposed to heating-cooling cycles between quasi room temperature and stepwise-increased high temperatures of 450 °C, 650 °C, and 800 °C, respectively. *In situ* RBS revealed full compositional stability of the SSC during thermal cycling. *In situ* SE indicated full conservation of the optical response at 450 °C and 650 °C, and minimal changes at 800 °C. The analysis of the *ex situ* optical reflectance spectra after the complete thermal cycling gave an unchanged solar absorptance of 0.94 and a slightly higher calculated thermal emittance at 800 °C of 0.16 compared to 0.15 after deposition. Cross-sectional element distribution analysis performed in scanning transmission electron microscopy mode confirmed the conservation of the SSC's microstructure after the heating – cooling cycles. The study demonstrates compositional, optical, and structural stability of the WAlSiN-based solar-selective coating at temperatures targeted for the next generation of concentrated solar power plants.

[1] Corresponding author
Email: harish@nal.res.in (H.C. Barshilia)

Keywords: Concentrated solar power, high-temperature solar-selective coatings, nanolaminates, *in situ* analysis, ion beam analysis, STEM-EDXS imaging

1. Introduction

Worldwide, energy consumption is rising with the rapid increase in industrialization and population. Since the climate change requires the replacement of fossil fuels such as coal, oil and gas, a massive increase of renewable energies is required in the world wide share of energy[1]. In this context, research groups are exploring the opportunities of renewable energy resources in establishing the large-scale production of electricity via photovoltaics and concentrated solar power plants (CSP, also termed solar thermal electricity)[2,3]. Researchers have widely explored the CSP technology regarding various aspects for improving the overall efficiency of the plants. The CSP technology has four major components: concentrator, solar receiver, heat transfer fluid, and power conversion system. In this technology, solar selective coatings (SSC) deposited on the receivers play a significant role in improving the overall efficiency of the system[4,5,6]. An ideal SSC should possess a high solar absorptance ($\alpha \geq 0.95$), low thermal emissivity ($\varepsilon \leq 0.10$), and thermal stability at high operating temperatures[7]. Up to now, SSCs deposited by PVD techniques are widely used in parabolic trough collectors, which operate at a working temperature (T) of $T \leq 400$ °C in vacuum[3].

Several research groups have investigated various potential materials for solar absorbers for high-temperature application in the past decade. Transition-metal-based absorbers, i.e., nitrides, oxynitrides and oxides demonstrate excellent resistance towards oxidation, chemical and corrosion properties and tuneable optical properties. Some of the high-temperature solar absorber coatings reported are: CrAlN/CrAlON/Al_2O_3, CrAlN/CrAlON/Si_3N_4[8], Ti/AlTiN/AlTiON/AlTiO[9], W/Ag/WN-AlN/AlN/SiO_2[10], AlMoN(H)/AlMoN(L)[11], W/$AlSi_xN$/$AlSiO_yN_x$/$AlSiO_x$[12], Mo/ZrSiN/ZrSiON/SiO_2[13],

W/CrAlSiN_x/CrAlSiN_xO_y/SiAlO_x[14], TiN/AlCrSiO/AlCrSiO[15], $Al_yTi_{1-y}(O_xN_{1-x})$ oxynitride multilayer[16,17], etc.. The literature shows that most solar absorber coatings developed for high-temperature applications degrade primarily due to oxidation, thermal stress and diffusion of the constituent elements in the coatings[18]. Moreover, with an increase in temperature, the thermal emissivity also increases, reducing the efficiency due to the loss of absorbed energy in the form of IR radiation (thermal dissipation)[19]. Furthermore, the structural and morphological changes, induced at high-temperature due to the degradation, affect the optical properties (α, ε and optical constants) and thermal emissivity of the coating. Therefore, it is necessary to understand the structural and compositional changes induced at high-temperature and the influence of these changes on the optical properties and thermal stability of the coating. In this context, recently, Escobar-Galindo et al. investigated the microstructure, element composition, chemical bonding, and optical properties of $Al_yTi_{1-y}(O_xN_{1-x})$ multilayers before and after single-stage (12 h) and thermal cycling treatments (900 h) at 450 °C, 650 °C, and 800 °C in air[17]. The results indicated the stability of the SSCs up to 650 °C. Only at 800 °C, a rutile-TiO_2 film formed on the surface, leading to the degradation of the coating[17]. In addition to these classical, *ex situ* stability studies comparing composition, structure, and properties of SSCs prior and after high-temperature treatments, new approaches towards the assessment of optical properties, composition, and structural changes are necessary by using *in situ* techniques. It is an essential question to clarify whether the optical properties, i.e. for CSP coatings the high absorptance and low emittance, are conserved at high temperatures or not. Dynamic processes might broaden the electronic states, increase damping and finally decrease the absorption intensity and blur out or shift the reflectivity edge. Intermixing of the sharp interlayers could appear at temperatures of up to 800 °C. Material losses are another possible reason of coating degradation. The onset-temperature of those effects can be only identified by *in situ* measurements. In this respect, Lungwitz et al. reported *in situ* spectroscopic ellipsometry (SE)

and Rutherford backscattering spectrometry (RBS) measurements up to 800 °C for 2 h in high vacuum for a SnO_2:Ta transparent conductive oxide coating, which can be used as selective transmitter coating on top of a blackbody absorber[20]. In spite of this report it is to be emphasized here that *in situ* measurements, using e.g. RBS and SE, are less explored in characterizing solar absorber materials[21,22]. However, these techniques are highly desirable since they can provide evidence for the conservation of the structural and optical properties of SSCs *in operando* at high temperatures (T > 600 °C), which correspond to those required for next generation CSP plants.

In the present work, we report such type of *in situ* studies for the WAlSiN-based spectrally-selective solar absorber coating. Its previously proposed layer stacking was W/WAlSiN/SiON/SiO_2, and durability tests under various conditions indicated stability in air up to 500 °C and in vacuum up to 700 °C for 200 h[23,24]. We have carried out *in situ* RBS and SE measurements during heating – cooling cycles between quasi room temperature (25 °C ≤ T ≤ 100 °C) and the three subsequently increased high temperatures of 450 °C, 650 °C, and 800 °C. The measurements were performed at the cluster tool facility located at the Ion Beam Center (IBC) of the HZDR[21,22,25]. In order to confirm the *in situ* results, the element composition, the optical and the microstructural properties of the solar absorber coating were evaluated using *ex situ* reflectance spectroscopy and cross-sectional, scanning transmission electron microscopy (STEM) including spectrum imaging analysis based on energy-dispersive X-ray spectroscopy (EDXS) before and after the high-temperature cycling. This analysis led to an improved stacking order and phase structure model of the SSC, which is consistent with the element concentrations. It moreover provides a profound understanding of the superior thermal and oxidation resistance of the studied SSC. Finally, the slight increase of the thermal emittance from $\varepsilon_{800\,°C}$ = 0.15 to 0.16 is tentatively attributed to an oxygen enrichment observed by STEM-EDXS on top of the absorber layer of the SSC. Our study demonstrate that the fabricated solar

absorber coating has excellent compositional, microstructural, and thermal stability up to 800 °C in vacuum during the entire heating-cooling cycling.

2. Experimental details

A four-cathode reactive unbalanced direct-current (DC) magnetron sputtering system with high purity (W, Al, and Si >99.9 %) targets was utilized to fabricate the WAlSiN-based solar-selective coating. The as-deposited samples were deposited on stainless-steel (SS) and silicon (Si) substrates for analysis. A distance of 10 cm between the target and substrate holder was kept constant throughout the deposition process. The substrates were cleaned by *in situ* Ar ion bombardment for 5 min at a bias voltage of -1000 V. The deposition of the solar absorber coatings was carried out at a constant substrate temperature of 200 ºC. A detailed discussion on the optimization of the process parameters used for the deposition of the WAlSiN-based solar absorber coatings is reported in our previous article[26]. Seven samples with *de facto* identical compositional, structural and optical properties were deposited in one batch for this study (see supporting information).

In situ RBS and SE investigations of the compositional and optical high-temperature stability of the SCCs were performed at the cluster tool of the IBC at the HZDR[25]. This setup is designed for processing and comprehensive characterization of thin films at high temperatures. Temperature-dependent *in situ* RBS was performed in a 155° backscattering geometry using 2 MeV He^+ ions with a beam current of approx. 20 nA. *In situ* SE was measured by using a Woollam M-2000 ellipsometer with a fixed angle of 70.5° in the spectral range from 371 to 1680 nm. For both *in situ* experiment series, a uniform heating – cooling cycle protocol was employed. It comprised the initial measurements at room temperature (RT), followed by three heating cooling cycles to 450 °C, 650 °C, and 800 °C, respectively and a cooling step

back to 100 °C, and a final measurement at RT (Figure 1). The time for the seven ramps, including the time for temperature stabilization was 30 min each, and so was the measurement time at each of the eight temperatures after thermal stabilization. This gives a total experiment duration of 7.5 h for the applied heating – cooling cycles.

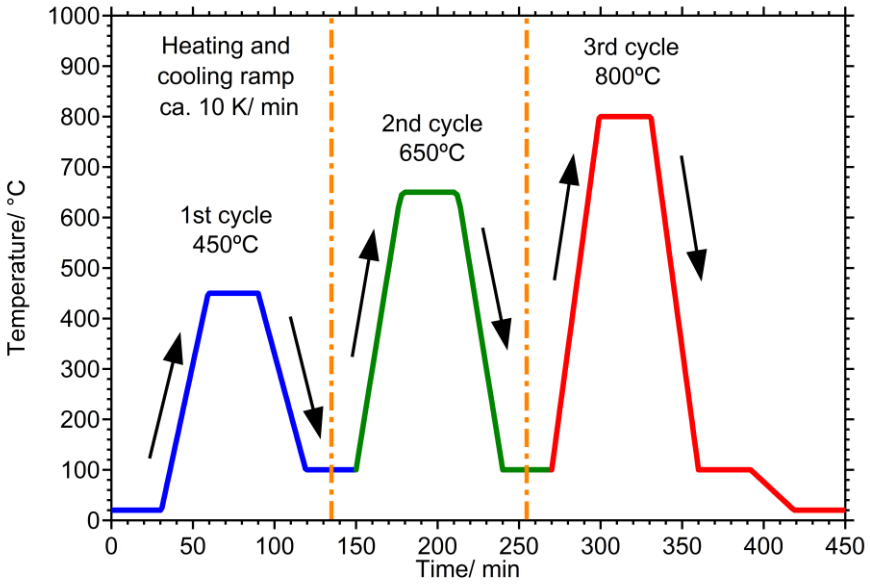

Figure 1: Graphical representation of the heating-cooling cycling protocol applied for *in situ* RBS and SE measurements of the WAlSiN-based SSC.

In addition to RBS, elastic recoil detection (ERD) was applied as complementary *in situ* ion beam analysis technique. For ERD, a 35 MeV Cl^{7+} ion beam was used. The angle between the sample normal and the incoming beam was 67.5° and the scattering angle was 45°. The analysed area was about 2.5 x 2.5 mm². The recoil atoms and scattered ions have been detected with a Bragg Ionisation Chamber (BIC), which enables energy measurement and Z identification of the particles (BP signal, BP = Bragg peak). Since the heavy Cl^{7+} ions caused some damage of the samples, only the ERD spectra taken at RT prior to the heating-cooling cycling were included in this study. All RBS and ERD spectra were fitted simultaneously using

the program NDF v9.6[27]. The accuracy of the as-obtained element concentrations is 1 at.%, and accordingly, all element concentrations are given as integer numbers in this article.

Ex situ optical reflectance spectra of the as-deposited and thermally-cycled samples were measured using a Shimadzu SolidSpec 3700 DUV spectrometer in the wavelength range of 250 – 3300 nm. The incidence angle was 5º relative to the surface normal. For measuring the reflectance of the samples in the infrared range from 2500 nm to 25 µm, a Bruker Vertex 80v spectrometer was applied with an incidence angle of 12°. The spectra of both ranges had a very good overlap and were merged for the calculation of the solar parameters. An M-2000 ellipsometer (Woollam) was used for the *ex situ* SE measurements in the range from 211 nm to 1688 nm. Three different angles of polarized light (*s* and *p*), 55°, 65°, and 75°, respectively, were applied to characterize the seven as-deposited samples of the same batch. Subsequently, the SE data and the reflectance data of all the seven as-deposited samples were combined in a coupled analysis in order to develop an optical spline model employing the CompleteEASE software (Woollam)[28,29]. The optical model describes the ellipsometric and reflectance data correctly and provides the refractive index, extinction coefficient, layer thicknesses and roughness of the studied SCC.

Cross-sectional TEM specimens of the SCCs were prepared by *in situ* lift-out using a Helios 5 CX focused ion beam (FIB) device (Thermo Fisher). To protect the sample surface, a carbon cap layer was deposited beginning with electron-beam-assisted and subsequently followed by Ga-FIB-assisted precursor decomposition. Afterwards, the TEM lamella was prepared using a 30-keV Ga-FIB with adapted currents. Its transfer to a 3-post copper lift-out grid (Omniprobe) was done with an EasyLift EX nanomanipulator (Thermo Fisher). To minimize sidewall damage, Ga ions with only 5 keV energy were used for final thinning of the TEM lamella to electron transparency. Cross-sectional bright-field and high-resolution TEM

imaging were performed using an image-C_s-corrected Titan 80-300 microscope (FEI) operated at an accelerating voltage of 300 kV. High-angle annular dark-field scanning transmission electron microscopy (HAADF-STEM) imaging and spectrum imaging analysis based on energy-dispersive X-ray spectroscopy (EDXS) were performed with a Talos F200X microscope (FEI) operated at 200 kV. Prior to (S)TEM analysis, the specimen mounted in a high-visibility low-background holder was treated for 8 s with a Model 1020 Plasma Cleaner (Fischione) to remove potential contaminations.

3. Results and discussion:

3.1 Stack composition and microstructure of the WAlSiN-based selective absorber prior to heating – cooling cycles

The element depth profiles of the as-deposited WAlSiN-based selective absorber obtained by NDF fits[27] of the *in situ* RBS and ERD data at room temperature are shown in Figure 2. The areal density in at/cm² is directly obtained from the analysis and is a measure of the film thickness. Four distinct layers are evident from the depth profile.

Table 1: Element composition of the four layers comprising the WAlSiN-based SSC prior to the heating – cooling cycling as obtained be in situ RBS + ERD. Minimal deviations (-1 at.%) from a sum of 100 at.% for the interlayer and the absorber layer result from the rounding of the concentrations obtained by the fitting to the realistic integer accuracy.

	W (at.%)	N (at.%)	Si (at.%)	Al (at.%)	O (at.%)
IR Layer	100	0	0	0	0
Interlayer	59	38	0	0	2
Absorber layer	14	47	18	8	12
AR layer	0	4	34	0	62

The infrared reflective layer (IR layer) consists of metallic W. A thin interlayer (IL) of the mean composition $W_{1.6}N$ is formed between the IR and the absorber layer. The absorber layer

is comprised of N (47 at.%), Si (18 at.%), W (14 at.%), O (12 at.%), and Al (8 at.%). Finally, the antireflective layer (AR layer) is best described by $SiO_{2-x}(N_y)$, since the N concentration drops rapidly to less than 5 at.% from the absorber/ AR layer interface towards the surface (Figure 2). The steep change in the W depth profile between IR layer and $W_{1.6}N$ interlayer is ascribed to the drastic change in the calculated stopping power between these constituent layers. The same holds for the sharp peak in the N profile between absorber and $W_{1.6}N$-IL. The ion beam analysis reveals new aspects of the element composition of the studied SSC. The $W_{1.6}N$ interlayer is detected for the first time, the presence of oxygen in the absorber layer is revealed, and a N-concentration gradient of the AR layer is demonstrated. The observation of oxygen in the absorber layer can be ascribed to the O content in the N_2 gas cylinder used during deposition since no O is observed in the W layer when pure Ar was used for deposition. On the other hand the fraction of approx. 12 at.% O must not affect the optical properties negatively and might even stabilize the absorber layer of the SSC.

It is tempting to estimate the composition of the absorber layer not only in terms of elements, but also in terms of chemical compounds or structural phases. We assume that all oxygen is preferentially bound to Al, since Al_2O_3 has the highest bonding energy among the possible structural phases, namely -3.28 eV/atom, followed by SiO_2 with -2.96 eV/atom[30]. Compared to them, the binary nitrides AlN and Si_3N_4 are energetically much less favourable with -1.49 eV/atom and -0.96 eV/atom, respectively[30]. We obtain an almost perfectly stoichiometric alumina, namely $Al_2O_{2.97}$. The remaining absorber layer elements are W, N and Si. Assuming now that SiN_x exists as stoichiometric Si_3N_4, the remaining WN_x would be definitively rich in N, with a tentative stoichiometry of approx. $WN_{1.6}$. From these estimations follows that tungsten nitride exists in different compositions in the studied SSC: as W-rich $W_{1.6}N$ interlayer (IL) between IR and absorber layer, and as N-rich tungsten nitride in the absorber layer. Both compositions are consistent with the binary W-N phase diagram,

according to which the hexagonal δ-WN phase is capable to adopt the estimated N-concentrations[31].

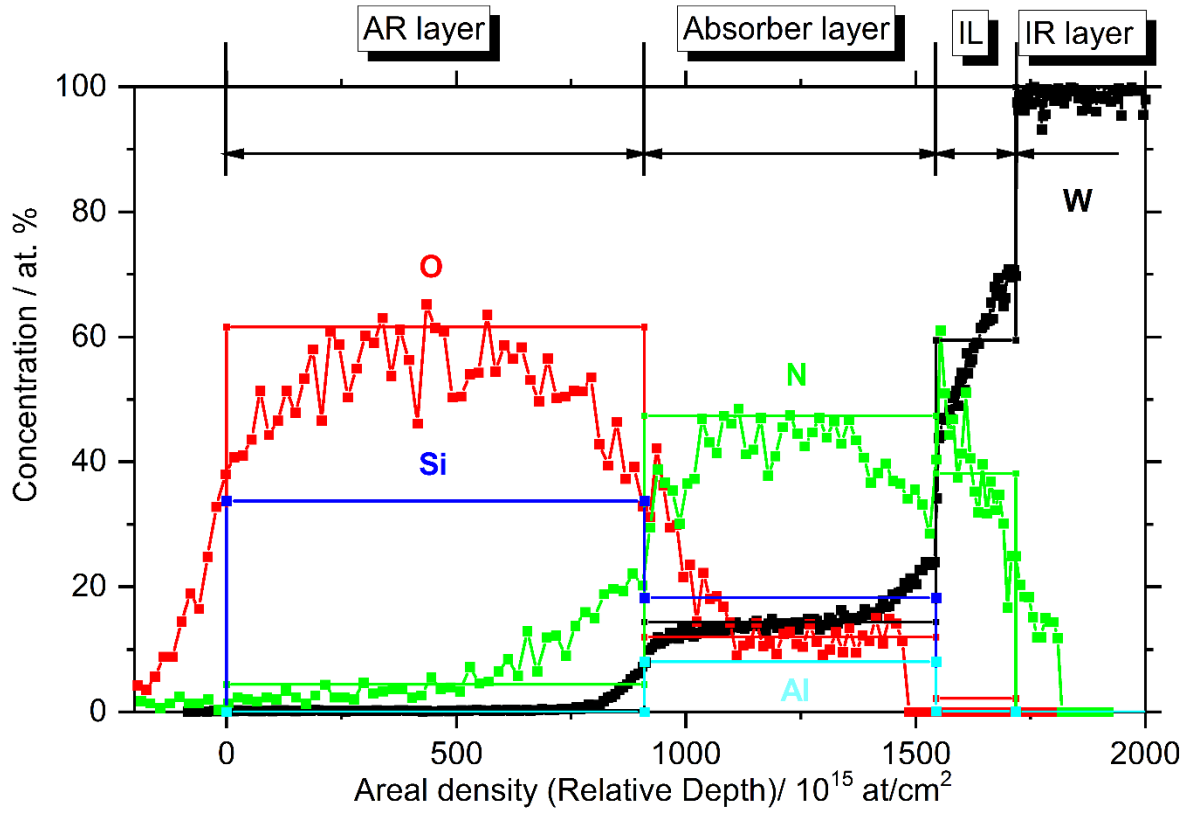

Figure 2: Element depth profile of the WAlSiN-based SSC stack prior to the heating - cooling cycles derived from RBS and ERD at RT. The curves are depth profiles directly extracted from the spectra and the straight lines are the sample model fitted to the spectra.

According to the above estimation, the absorber layer consists of three structural phases, namely 21 mol% $Al_2O_{2.97}$, 42 mol% Si_3N_4, and 37 mol% $WN_{1.6}$. According to this composition, the concentration ratio of light- (low-Z) and heavy-element containing (high-Z) structural phases is approx. 1.7/1. This is reflected in the volume fractions visualized by cross-sectional TEM-based analysis later on. The following table (Figure 3) illustrates the assignment of the overall element composition to the individual compounds (structural phases) of the absorber layer.

Table 2: Assignment of the element composition obtained by ERD + RBS to the structural phases of the as-deposited WAlSiN-based absorber layer of the studied SSC.

	Element concentrations of the absorber layer					
	W (at. %)	N (at.%)	Si (at.%)	Al (at.%)	O (at.%)	Sum (at.%)
Total	14	47	18	8	12	100
Rest after subtracting $Al_2O_{2.97}$	14	47	18	0	0	79
Rest after subtracting Si_3N_4	14	0	23	0	0	37
Rest after subtracting $WN_{1.6}$	0	0	0	0	0	0

Cross-sectional TEM micrographs and STEM-EDXS-based element analysis confirm the stacking sequence of the as-deposited WAlSiN-based selective absorber concluded from the RBS and ERD analysis. In particular, bright-field TEM (Figure 3a) and HAADF-STEM images (Figure 3b) clearly show four distinct layers with different image contrast, which correspond to the IR layer of W, the $W_{1.6}N$ IL, the absorber and the AR layer, respectively. The absorber layer consists of a periodic nanolaminate of 19 high-Z and 20 low-Z (Z: atomic number) layers, i.e., bottom and top nanolaminate layers have low-Z nature. The low-Z layers have a thickness of approx. (2.3±0.1) nm compared to approx. (1.7±0.1) nm for the high-Z layers. This ratio is almost the same as the molar ratio of low-Z to high-Z absorber phases obtained above. In order to verify the absorber layer phases deduced from ERD and RBS, spectrum imaging analysis based on energy-dispersive X-ray spectroscopy (EDXS) was performed (Figure 3). Particular attention was laid on the N- and O-containing phases, since our study delivers new insights regarding to them. Figure 3c shows the distribution of N, Al and Si in the full layer stack. N is present in the $W_{1.6}N$ interlayer and in both absorber nanolaminate layers. In the AR layer, very few N is found. Its quantity is of the noise level of the figure. Al and Si are found in one absorber nanolaminate layer together with N but not in the other. The AR layer contains Si and no Al, and as already mentioned, very few N. Figure

3d reveals the distribution of W and N in the absorber layer. One of the nanolaminate layers contains W and N, the other only N. The relative intensity of N is higher in the former, and lower in the latter. This finding supports the ion beam analysis data evaluation, according to which the high-Z $WN_{1.6}$ nanolaminate layers contain 62 at.% N and those of the low-Z nanolaminate only 38 at.% N. Figure 3d moreover confirms the sharp drop of the N-concentration above the absorber layer. Figure 3e illustrates the distribution of Al and Si in the absorber layer. Both are only present in the low-Z nanolaminate layer. Finally, Figure 3f reveals the periodic O-concentration in the absorber along with Si (and Al), in full agreement with the proposed formation of Al_2O_3 in the low-Z nanolaminate layer and the onset of the continuous O-distribution in the AR layer.

The obtained STEM-EDXS results are in full agreement with the RBS and ERD analysis of the as-deposited WAlSiN-based solar-selective coating. In conclusion, the absorber layer is better described as WAlSiN(O) than as WAlSiN. However, to avoid confusion, the originally-proposed terminus WAlSiN is used further on. The previously proposed nanolaminate microstructure of the absorber layer was confirmed[23]. It is comprised of alternating low-Z and high-Z layers. For the high-Z laminate layer a stoichiometry of $WN_{1.6}$ is deduced. Moreover, we propose that the low-Z laminate layer comprises the main structural phases Al_2O_3 and Si_3N_4. A low-Z laminate layer forms the upper edge of the absorber, and provides the platform for the growth of the AR layer. Therein, the N contents drops rapidly to less than 5 at.%, and stoichiometric SiO_2 is formed as the dominant constituent of it.

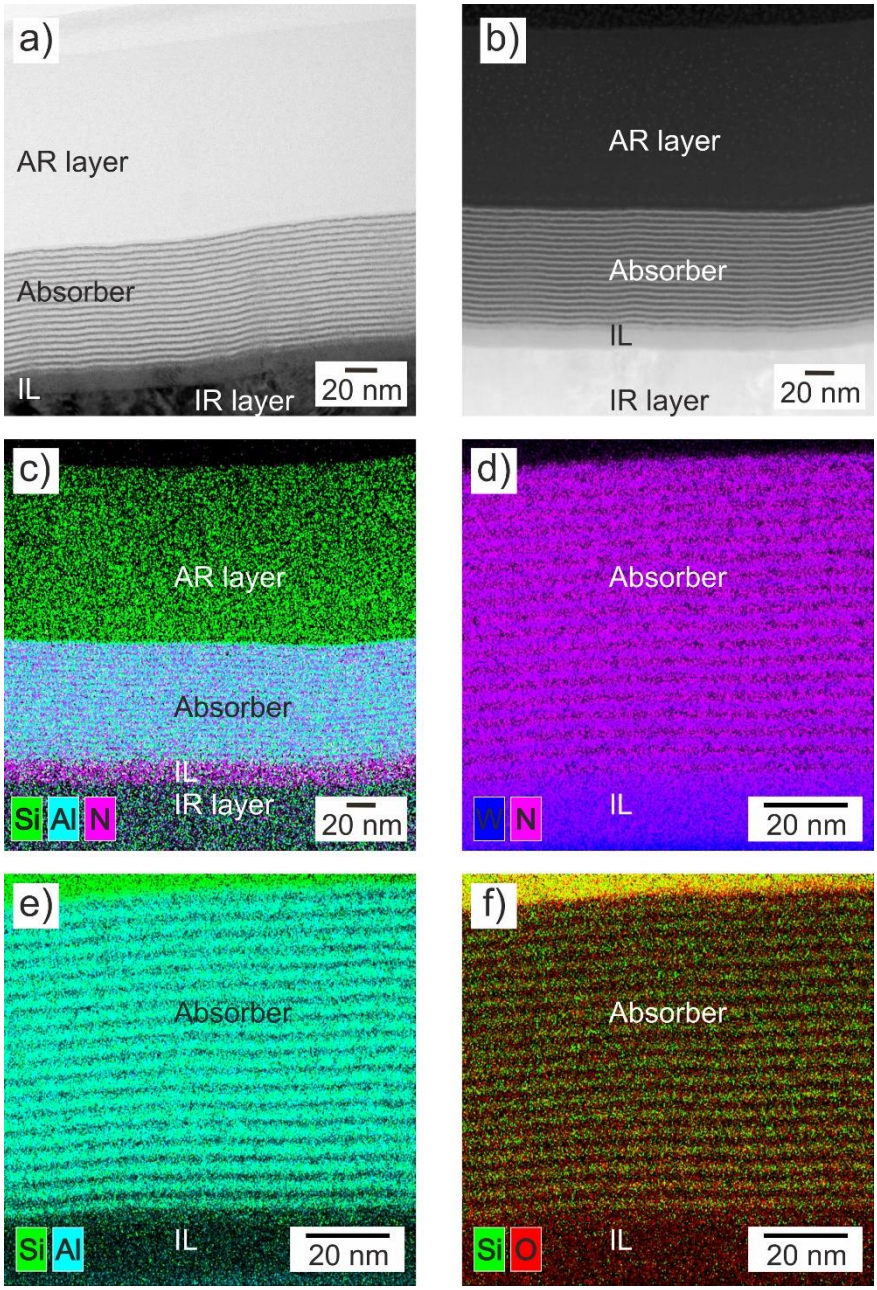

Figure 3: TEM-based micrographs of the SSC after deposition. a) bright-field TEM and b) HAADF-STEM image displaying the AR coating, absorber layer, interlayer (IL), and IR reflector (from top to bottom); Distribution maps of selected elements measured by STEM-EDXS in all four stack layers (c)) and in the absorber layer (d)-f)).

3.2 *In situ* RBS and SE evidence of compositional and optical stability of the WAlSiN-based selective absorber stack during heating – cooling cycles up to 800 °C

The conservation of their compositional and optical properties is crucial for the use of SSCs in high-temperature CSP applications. Ideally, this can be demonstrated *in situ* under conditions of high-temperature cycling. As explained in the introductory section, intermixing of layers or outwards diffusion of volatile constituents can change the optimized layer stacking and reduce the optical performance of SSCs. Therefore, the compositional and optical stability of the WAlSiN-based SSC was investigated by *in situ* RBS and SE during an identical heating – cooling cycling protocol (see section 2 and Figure 1). The three different high-temperature treatments - 450 °C, 650 °C, and 800 °C - correspond to the current operation temperature of parabolic trough solar power plants, the current high-temperature limit of solar central receiver plants and the target temperature of the next-generation CSP plants, respectively[32,1]. Selected *in situ* RBS spectra taken during the experiment are displayed in Figure 4. The edges of the SSC elements W, Si (Al cannot be separated from Si), O and N are identified at all temperatures with apparently the same intensity. Most importantly, the room temperature *in situ* RBS spectrum measured before and after the heating - cooling cycling is unchanged, as it is shown in the inset of Figure 4. The Fe edge is caused by the stainless steel substrate. The conservation of the Fe edge energy is a clear indicator for the mass conservation of the SSC during the heating – cooling cycling. Otherwise, the substrate edge would have shifted to higher or lower backscattering energies, indicating mass loss or gain, respectively.

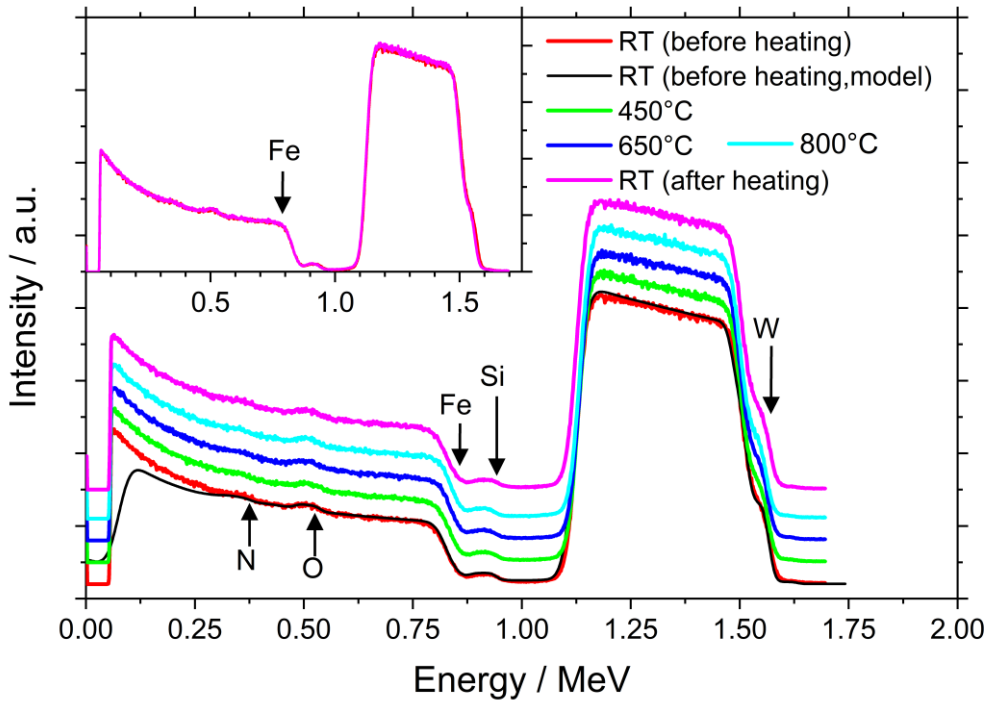

Figure 4 : *In situ* RBS spectra of W/WAlSiN/SiON/SiO_2 SSC stack taken during the heating – cooling cycles.

Even though the *in situ* RBS technique is very powerful in demonstrating the conservation of element composition, stacking order, and total mass, it does not proof the conservation of the SSC's optical properties at high temperatures. Therefore, *in situ* SE was performed during the same heating - cooling cycling protocol. The ellipsometric parameters Ψ (Psi) and Δ (Delta) are plotted separately as a function of temperature in Figure 5a and Figure 5b, respectively. In both graphs, the solid lines represent the measurements at low temperatures (25 °C, 100 °C and 25 °C) and dotted lines represent the measurements at high temperatures (450 °C, 650 °C and 800 °C). In the Psi spectra taken at 450 °C and 650 °C, the two maxima are slightly shifted to shorter wavelengths (blue-shifted) compared to the spectra taken at 25 °C and 100 °C. These shifts are reversed when the samples are cooled down to 100 °C, indicating that they reflect minor reversible changes of the optical properties at 450 °C and 650 °C. Similar reversible changes are seen in the Delta spectra taken at 450 °C and 650 °C (Figure

5b). At 800 °C, the changes in the Psi and Delta spectra are larger than at 450 °C and 650 °C, and they are not fully reversible anymore. However, the general signature of the ellipsometric data is retained even at this very high temperature, and it shows the conservation of the solar-selective properties of the studied WAlSiN-based solar absorber.

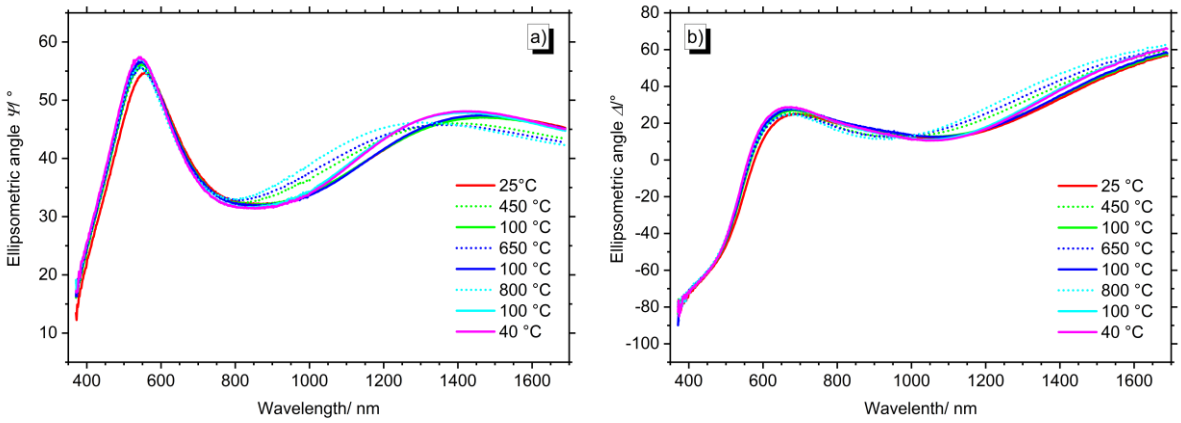

Figure 5: *In situ* SE spectra of W/WAlSiN/SiON/SiO_2 SSC stack taken during the heating – cooling cycles.

3.3 Post heating – cooling cycling proof of optical and microstructural stability of the WAlSiN-based selective absorber stack

3.3.1 Optical properties of WAlSiN-based selective absorber stack prior to and after heating – cooling cycling

After the initial composition and microstructure of the studied WAlSiN-based solar absorber were clarified (section 3.1) and *in situ* RBS and SE experiments have demonstrated its compositional and optical stability at high temperatures (section 3.2), the solar parameters of the SSC prior to and after the heating – cooling cycling were determined. Therefore, the optical reflectance spectra were measured in the wavelength range of 0.25-25 µm and the solar absorptance (α) and thermal emissivity (ε) for 800 °C were calculated from them (Figure 6).

The reflectance spectra of a selected WAlSiN-based solar absorber sample prior to and after the heating and cooling cycling experiment are presented in Figure 6. The signatures of both are highly solar-selective, with approx. 4 % reflectance (approx. 96 % absorptance) in the visible and approx. 95 % reflectance in the thermal range. After the heating – cooling cycling, the reflectance in the range between 400 nm and 500 nm is slightly lower (approx. 1 %), and the infrared reflectance is by approx. 1 % reduced. This means, the sample would absorb little more sunlight, but also emit little more thermal radiation. Quantitatively, the differences are negligible. The as-deposited sample exhibits a solar absorptance of 0.94 and a thermal emissivity of 0.15 (@ T = 800 °C). The heating-cooling cycled sample has the same solar absorptance ($\Delta\alpha = 0$) and a slightly higher thermal emissivity ($\Delta\varepsilon_{800\,°C} = +\,0.1$) (Figure 6). Thus, the reflectance spectra and the solar parameter values are clear evidence of the high optical stability of the WAlSiN-based solar absorber under high-temperature heating-cooling cycling. They are in full agreement with the *in situ* SE studies presented in the previous section.

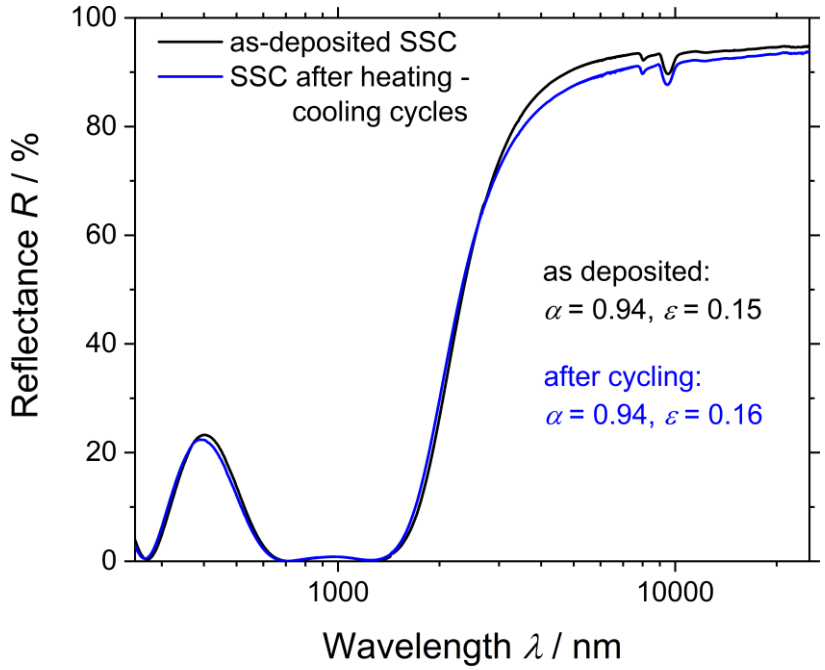

Figure 6: UV-Vis-IR reflectance spectra of the W/WAlSiN/SiON/SiO_2 SSC stack prior to and after the heating – cooling cycles with data calculated for the solar absorptance and the thermal emittance at 800 °C.

Based on the reflectance spectra and the *ex situ* SE data the optical constants of the as-deposited SSC were estimated (see Figure 7). The experimentally measured (open circle) and the simulated data (black lines) are in excellent agreement, showing the robustness of the optical model. The simulated optical spline model is based on the following SSC stack structure: W - IR layer (265 nm)/ IL (15 nm)/ WAlSiN (81 nm)/ SiO_2 (119 nm) (Table 3). The inset in Fig. 7 (left panel) presents the refractive index (*n*) and extinction coefficient (*k*) of the WAlSiN layer. The decreasing trend in refractive index with increase in wavelength depicts the typical behavior of a semiconductor. The function of the extinction coefficient indicates that the absorber layer of the SCC absorbs in the whole spectral range from 300 nm to 1700 nm.

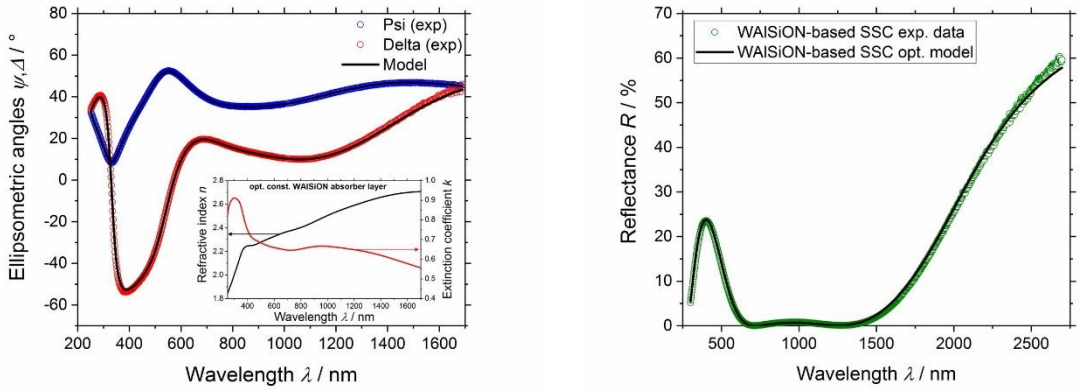

Figure 7: Experimental data of the SSC (open circles) and simulated data (black lines) developed in a coupled analysis of (left) SE and (right) reflectance measurements of all 7 SSCs. The inset of the left figure shows the optical constants of the WAlSiN-based absorber layer resulting from the optical model.

3.3.2 Proof of the microstructural stability of WAlSiN-based selective absorber stack after heating – cooling cycling

Cross-sectional TEM-based analysis provided detailed insight in the stacking sequence and the layer composition of the studied WAlSiN-based selective absorber stack (section 3.1). The same approach was applied to analyse these microstructural properties of the SSC after the high-temperature heating – cooling cycling. As the as-deposited stack, the thermally-cycled SSC consists of four principal layers (Figure 8). The nanolaminate microstructure of the absorber layer was conserved. For a more quantitative comparison, the thicknesses of the stacks obtained by modelling of the SE data and by the XTEM imaging are compiled in Table 3.

Table 3: Thicknesses of the four principal layers of the WAlSiN-based SSC prior to and after heating – cooling cycling up to 800 °C in high vacuum. The cross-sectional TEM values were averaged when more than one lamella was prepared.

Sample	Layer	d_{TEM} (nm)	d_{SE} (nm)
SSC – as deposited	AR layer	118 ± 3	119 ± 1
	Absorber	80 ± 1	81 ± 1
	IL	13 ± 1	15 ± 1
	IR reflector	263 ± 1	265 (not fitted)
SSC – after cycling	AR layer	120 ± 1	123 ± 1
	Absorber	78 ± 1	81 ± 1
	IL	11 ± 1	12 ± 1
	IR reflector	270 ± 3	265 (not fitted)

Foremost, we note a perfect agreement of the thickness values obtained by the two different techniques within the experimental accuracy. Comparing the thicknesses of the four SSC components prior to and after the heating – cooling cycling, only minor temperature-

induced thickness changes are found. Specifically, the AR layer seems to have grown by approx. 3 nm, and the IL has lost approx. 1 nm. The absorber layer thickness is unchanged within the experimental accuracy. The thicknesses of the nano laminate layers of the absorber layer are (2.2±0.1) nm and (1.6±0.1) nm for the low-Z and the high-Z component, respectively. Before the heating – cooling cycling the values were (2.3±0.1) nm and (1.7±0.1) nm, i.e., also this structure parameter is unchanged within the experimental accuracy. Its periodic pattern is regular after cycling, without local or extended damages (Figure 8). As after deposition, the upper nanolaminate layer of the absorber is a low-Z layer. The heating – cooling cycling did not induce changes in the element distribution of the SSC, even not in the absorber layer nanolaminate (Figure 8c) to Figure 8f)). All the element signatures discussed in detail in section 3.1 are conserved. Specifically, we note that N does not out-diffuse from the absorber into the AR layer and that the periodic N-concentration in the absorber is not equilibrated. The O-periodicity in the absorber layer is also conserved, and there is no O enrichment at the bottom of the absorber layer detected. This excludes the oxidation of $WN_{1.6}$ or W during the heating-cooling cycles, which might have occurred due to O diffusion from the absorber or AR layer. The only indication of a change in the O profile compared to the state prior to the heating – cooling cycling is the enhanced O signal intensity on top of the absorber. Finally, the cross-sectional TEM analysis indicate the thermal stability of the solar absorber coating during heating-cooling cycling up to 800 °C.

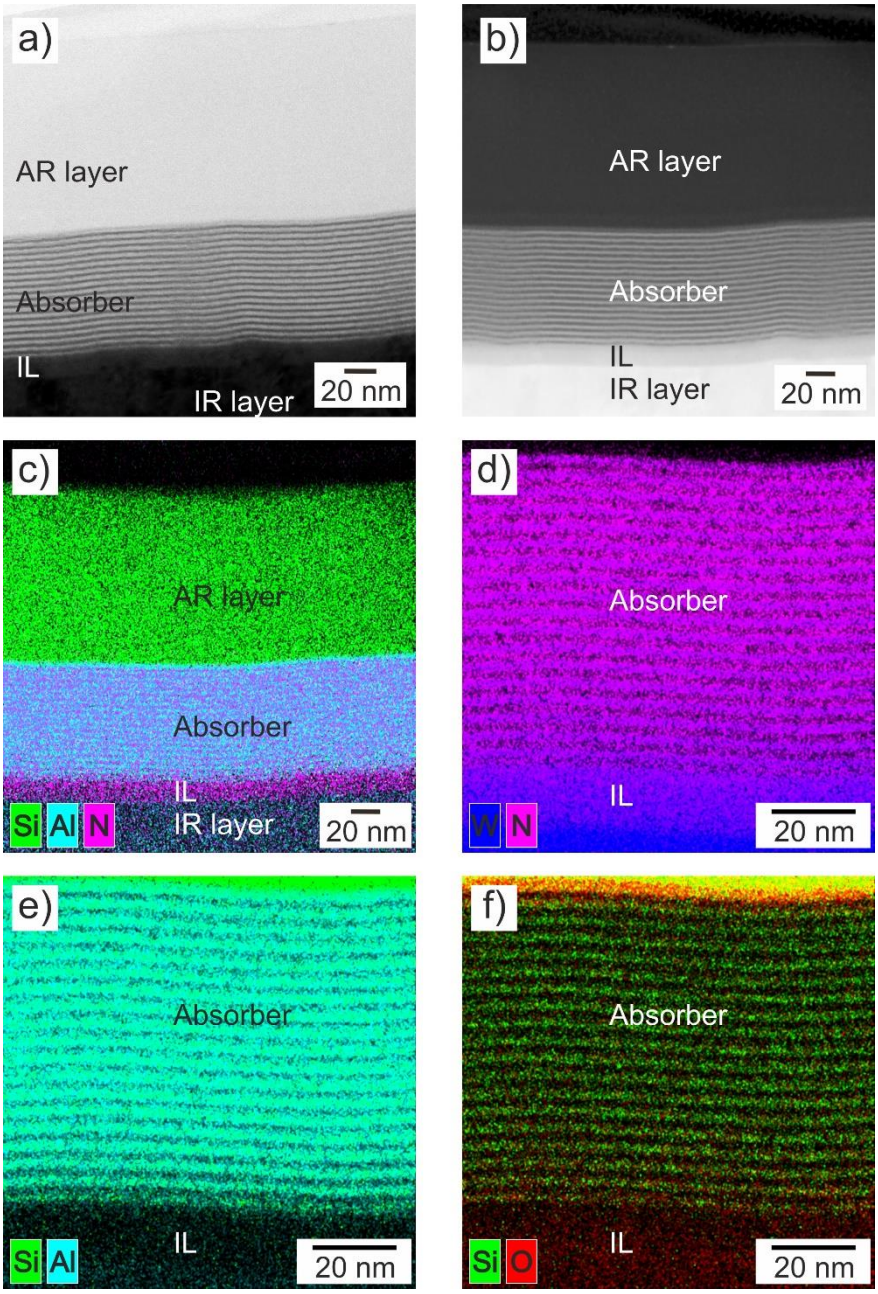
a)
AR layer
Absorber
IL
IR layer
20 nm
b)
AR layer
Absorber
IL
IR layer
20 nm
c)
AR layer
Absorber
IL
IR layer
Si
Al
N
20 nm
d)
Absorber
IL
W
N
20 nm
e)
Absorber
IL
Si
Al
20 nm
f)
Absorber
IL
Si
O
20 nm

Figure 8: TEM-based micrographs of the SSC after heating - cooling cycling up to 800 °C in vacuum. a) bright-field TEM and b) HAADF-STEM image displaying the AR layer, absorber layer, interlayer and IR layer (from top to bottom); Distribution maps of selected elements measured by STEM-EDXS in the four stack layers (c)) and in the absorber layer (d)-f)).

4. Conclusions:

In situ Rutherford Backscattering Spectrometry and Spectroscopic Ellipsometry were used to demonstrate the conservation of the compositional and optical properties of WAlSiN-based solar-selective coating during heating-cooling cycling up to 800 °C in high vacuum. The *in situ* results are verified by *ex situ* ion beam analysis, reflectometry, SE and cross-sectional TEM-based analysis prior to and after the thermal treatment. The element composition of the SSC was determined for the first time, and based on that, its stacking sequence was revised. The stacking structure comprises the tungsten IR-layer, a $W_{1.6}N$ interlayer, the absorber nanolaminate and the AR layer of almost pure SiO_2. The high concentration of non-metals – 47 at.% N and 12 at.% O – made the revision of the previously proposed structural phases of the absorber nanolaminate necessary. The low-Z (Z: atomic number) absorber layer consists presumably of $Al_2O_{2.97}$ and Si_3N_4, while the high-Z absorber phase is constituted of $WN_{1.6}$. In conclusion, the studied SSC has a richer phase structure than originally expected, what might account for its superior solar-selectivity. Its excellent high-temperature and oxidation stability can now be at least partially attributed to the presence of oxidation-resistant oxides in the low-Z absorber layers, which sandwich the high-Z $WN_{1.6}$ absorber layers responsible for the high absorptance.

The minor changes observed during *in situ* SE and in the reflectance and SE spectra of the thermally-cycled sample are not fully understood so far, since neither the stacking order, nor the individual layer thicknesses or the element composition showed a significant change. The only observed change in the coating architecture was a moderate O-enrichment on top of the absorber layer. It might cause additional scattering, slightly reducing the optical reflectance. However, its influence on the solar parameters is minor: The solar absorptance did not change at all (α = 0.94), and the thermal emittance, $\varepsilon_{800\,°C}$, increased only from 0.15 to 0.16. The results obtained demonstrate the superior compositional and structural stability and optical performance up to a temperature of 800°C in vacuum. These results suggest the SSC of the present work as a potential candidate for high-temperature CSP applications.

Acknowledgements

HCB thanks the Indo-French Centre for the Promotion of Advanced Research (CEFIPRA), New Delhi, India and Department of Science and Technology, New Delhi, India for partial funding support to carry out high-temperature solar absorber coating work at CSIR-NAL. K. Niranjan thanks CSIR for providing CSIR-SRF fellowship. Support by the Ion Beam center (IBC) of the HZDR and the Structural Characterization Facilities Dresden-Rossendorf at IBC is gratefully acknowledged. Moreover, we thank C. Habenicht, A. Garcia-Valenzuela, R. Heller, R. Aniol, A. Kunz, E. Christalle, A. Schneider (all HZDR) for technical support.

References:

(1) Escobar-Galindo, R.; Krause, M.; Niranjan, K.; Barshilia, H. C. Chapter 13: Solar Selective Coatings and Materials for High-Temperature Solar Thermal Applications. In *Sustainable Material Solutions for Solar Energy Technologies*; 2022; pp 383–427.

(2) Baharoon, D. A.; Rahman, H. A.; Omar, W. Z. W.; Fadhl, S. O. Historical Development of Concentrating Solar Power Technologies to Generate Clean Electricity Efficiently – A Review. *Renew. Sustain. Energy Rev.* **2015**, *41*, 996–1027. https://doi.org/10.1016/j.rser.2014.09.008.

(3) Pitz-Paal, R. Solar Energy – Concentrating Solar Power. In *Future Energy*; Elsevier, 2014; pp 405–431. https://doi.org/10.1016/B978-0-08-099424-6.00019-3.

(4) Barlev, D.; Vidu, R.; Stroeve, P. Innovation in Concentrated Solar Power. *Sol. Energy Mater. Sol. Cells* **2011**, *95* (10), 2703–2725. https://doi.org/10.1016/j.solmat.2011.05.020.

(5) Weinstein, L. A.; Loomis, J.; Bhatia, B.; Bierman, D. M.; Wang, E. N.; Chen, G. Concentrating Solar Power. *Chem. Rev.* **2015**, *115* (23), 12797–12838. https://doi.org/10.1021/acs.chemrev.5b00397.

(6) Atkinson, C.; Sansom, C. L.; Almond, H. J.; Shaw, C. P. Coatings for Concentrating Solar Systems - A Review. *Renew. Sustain. Energy Rev.* **2015**, *45*, 113–122. https://doi.org/10.1016/j.rser.2015.01.015.

(7) Kennedy, C. E. *Review of Mid- to High-Temperature Solar Selective Absorber Materials*; Golden, CO, 2002. https://doi.org/10.2172/15000706.

(8) Zou, C.; Huang, L.; Wang, J.; Xue, S. Effects of Antireflection Layers on the Optical and Thermal Stability Properties of a Spectrally Selective CrAlN–CrAlON Based Tandem Absorber. *Sol. Energy Mater. Sol. Cells* **2015**, *137*, 243–252. https://doi.org/10.1016/j.solmat.2015.02.010.

(9) Barshilia, H. C. Growth, Characterization and Performance Evaluation of Ti/AlTiN/AlTiON/AlTiO High Temperature Spectrally Selective Coatings for Solar Thermal Power Applications. *Sol. Energy Mater. Sol. Cells* **2014**, *130*, 322–330. https://doi.org/10.1016/j.solmat.2014.07.037.

(10) Antonaia, A.; Addonizio, M. L.; Esposito, S.; Ferrara, M.; Castaldo, A.; Guglielmo, A.; D'Angelo, A. Adhesion and Structural Stability Enhancement for Ag Layers Deposited on Steel in Selective Solar Coatings Technology. *Surf. Coatings Technol.* **2014**, *255*, 96–101. https://doi.org/10.1016/j.surfcoat.2014.02.045.

(11) Selvakumar, N.; Rajaguru, K.; Gouda, G. M.; Barshilia, H. C. AlMoN Based Spectrally Selective Coating with Improved Thermal Stability for High Temperature Solar Thermal Applications. *Sol. Energy* **2015**, *119*, 114–121. https://doi.org/10.1016/j.solener.2015.06.047.

(12) Rebouta, L.; Sousa, A.; Capela, P.; Andritschky, M.; Santilli, P.; Matilainen, A.; Pischow, K.; Barradas, N. P.; Alves, E. Solar Selective Absorbers Based on Al2O3:W Cermets and AlSiN/AlSiON Layers. *Sol. Energy Mater. Sol. Cells* **2015**, *137*, 93–100. https://doi.org/10.1016/j.solmat.2015.01.029.

(13) Ning, Y.; Wang, W.; Wang, L.; Sun, Y.; Song, P.; Man, H.; Zhang, Y.; Dai, B.; Zhang, J.; Wang, C.; et al. Optical Simulation and Preparation of Novel

Mo/ZrSiN/ZrSiON/SiO 2 Solar Selective Absorbing Coating. *Sol. Energy Mater. Sol. Cells* **2017**, *167* (March), 178–183. https://doi.org/10.1016/j.solmat.2017.04.017.

(14) AL-Rjoub, A.; Rebouta, L.; Costa, P.; Barradas, N. P.; Alves, E.; Ferreira, P. J.; Abderrafi, K.; Matilainen, A.; Pischow, K. A Design of Selective Solar Absorber for High Temperature Applications. *Sol. Energy* **2018**, *172*, 177–183. https://doi.org/10.1016/j.solener.2018.04.052.

(15) Yang, D.; Zhao, X.; Liu, Y.; Li, J.; Liu, H.; Hu, X.; Li, Z.; Zhang, J.; Guo, J.; Chen, Y.; et al. Enhanced Thermal Stability of Solar Selective Absorber Based on Nano-Multilayered AlCrSiO Films. *Sol. Energy Mater. Sol. Cells* **2020**, *207* (November 2019), 110331 (1-7). https://doi.org/10.1016/j.solmat.2019.110331.

(16) Heras, I.; Guillén, E.; Lungwitz, F.; Rincón-Llorente, G.; Munnik, F.; Schumann, E.; Azkona, I.; Krause, M.; Escobar-Galindo, R. Design of High-Temperature Solar-Selective Coatings Based on Aluminium Titanium Oxynitrides AlyTi1−y(OxN1−x). Part 1: Advanced Microstructural Characterization and Optical Simulation. *Sol. Energy Mater. Sol. Cells* **2018**, *176* (December), 81–92. https://doi.org/10.1016/j.solmat.2017.10.015.

(17) Escobar-Galindo, R.; Guillén, E.; Heras, I.; Rincón-Llorente, G.; Alcón-Camas, M.; Lungwitz, F.; Munnik, F.; Schumann, E.; Azkona, I.; Krause, M. Design of High-Temperature Solar-Selective Coatings Based on Aluminium Titanium Oxynitrides AlyTi1-y(OxN1-x). Part 2: Experimental Validation and Durability Tests at High Temperature. *Sol. Energy Mater. Sol. Cells* **2018**, *185* (April), 183–191. https://doi.org/10.1016/j.solmat.2018.04.027.

(18) Ibrahim, K.; Taha, H.; Rahman, M. M.; Kabir, H.; Jiang, Z. T. Solar Selective Performance of Metal Nitride/Oxynitride Based Magnetron Sputtered Thin Film Coatings: A Comprehensive Review. *Journal of Optics (United Kingdom)*. March 1, 2018, p 033001. https://doi.org/10.1088/2040-8986/aaa2c5.

(19) Kennedy, C. E. PROGRESS TO DEVELOP AN ADVANCED SOLAR-SELECTIVE COATING. **2012**, No. March 2008, 4–7.

(20) Lungwitz, F.; Escobar-Galindo, R.; Janke, D.; Schumann, E.; Wenisch, R.; Gemming, S.; Krause, M. Transparent Conductive Tantalum Doped Tin Oxide as Selectively Solar-Transmitting Coating for High Temperature Solar Thermal Applications. *Sol. Energy Mater. Sol. Cells* **2019**, *196* (February), 84–93. https://doi.org/10.1016/j.solmat.2019.03.012.

(21) Wenisch, R.; Lungwitz, F.; Hanf, D.; Heller, R.; Zscharschuch, J.; Hübner, R.; von Borany, J.; Abrasonis, G.; Gemming, S.; Escobar-Galindo, R.; et al. Cluster Tool for In Situ Processing and Comprehensive Characterization of Thin Films at High Temperatures. *Anal. Chem.* **2018**, *90* (13), 7837–7842. https://doi.org/10.1021/acs.analchem.8b00923.

(22) Krause, M.; Sonnenberg, J.; Munnik, F.; Grenzer, J.; Hübner, R.; Garcia-Valenzuela, A.; Gemming, S. *Formation, Structure, and Optical Properties of Copper Chromite Thin Films for High-Temperature Solar Absorbers*; Elsevier B.V., 2021; Vol. 18. https://doi.org/10.1016/j.mtla.2021.101156.

(23) Niranjan, K.; Soum-Glaude, A.; Carling-Plaza, A.; Bysakh, S.; John, S.; Barshilia, H. C. Extremely High Temperature Stable Nanometric Scale Multilayer Spectrally

Selective Absorber Coating: Emissivity Measurements at Elevated Temperatures and a Comprehensive Study on Ageing Mechanism. *Sol. Energy Mater. Sol. Cells* **2021**, *221* (November 2020), 110905. https://doi.org/10.1016/j.solmat.2020.110905.

(24) Niranjan, K.; Plaza, A. C.; Grifo, T.; Bordas, M.; Soum-Glaude, A.; Barshilia, H. C. Performance Evaluation and Durability Studies of W/WAlSiN/SiON/SiO2 Based Spectrally Selective Solar Absorber Coating for High-Temperature Applications: A Comprehensive Study on Thermal and Solar Accelerated Ageing. *Sol. Energy* **2021**, *227* (September), 457–467. https://doi.org/10.1016/j.solener.2021.09.026.

(25) Dresden-Rossendorf. HZDR. User facilities at the Ion Beam Center. https://www.hzdr.de/db/Cms?pOid=29003&pNid=1984.

(26) Niranjan, K.; Kondaiah, P.; Srinivas, G.; Barshilia, H. C. Optimization of W/WAlSiN/SiON/SiO2 Tandem Absorber Consisting of Double Layer Anti-Reflection Coating with Broadband Absorption in the Solar Spectrum Region. *Appl. Surf. Sci.* **2019**, *496*. https://doi.org/10.1016/j.apsusc.2019.143651.

(27) Barradas, N. P.; Jeynes, C.; Webb, R. P. Simulated Annealing Analysis of Rutherford Backscattering Data. *Appl. Phys. Lett.* **1997**, *71* (2), 291–293. https://doi.org/10.1063/1.119524.

(28) Wagner T. CompleteEase ellipsometry software online course QD Europe: Darmstadt, Germany. https://qd-europe.com/pl/en/events/event-details/completeease-course-online-training-2020/.

(29) Harland G. Tompkins; James N. Hilfiker. SPECTROSCOPIC ELLIPSOMETRY - Practical Application to Thin Film Characterization. In *Momentum Press: New York*; 2015.

(30) Jean d'Ans; Ellen Lax. Taschenbuch Für Chemiker Und Physiker, Band III: Elemente, Anorganische Verbindungen Und Materialien, Minerale. In *Springer Berlin Heidelberg*; 1998; p Vol. III.

(31) Villars, P.; Okamoto, H. N-W Binary Phase Diagram 30-100 at.% W: Datasheet from "PAULING FILE Multinaries Edition – 2012" in SpringerMaterials (https://materials.springer.com/isp/phase-diagram/docs/c_0904731).

(32) Loureiro, T.; Sterling, R.; Testani, C.; Torralba-Calleja, E.; Turchetti, L.; Blanco, M.; Ferriere, A.; Perrotta, F. Next Generation of Concentrated Solar Power Technologies. In *Sustainable Places 2019*; MDPI: Basel Switzerland, 2019; p 7. https://doi.org/10.3390/proceedings2019020007.

Supporting Information

The reflectance spectra of the whole batch of seven as-deposited samples (SSC #1 to SSC #7) are similar with very small differences of the order of $\Delta R = \pm 1\%$, indicating the high reproducibility of the sputtering process (see Figure S-1). Overall differences in optical reflectance and optical selectivity of the different solar absorber coatings are minor and, thereby, will have an insignificant impact on the performance of the coating. Therefore, the samples from the same deposition batch can be considered as equivalent for various studies.

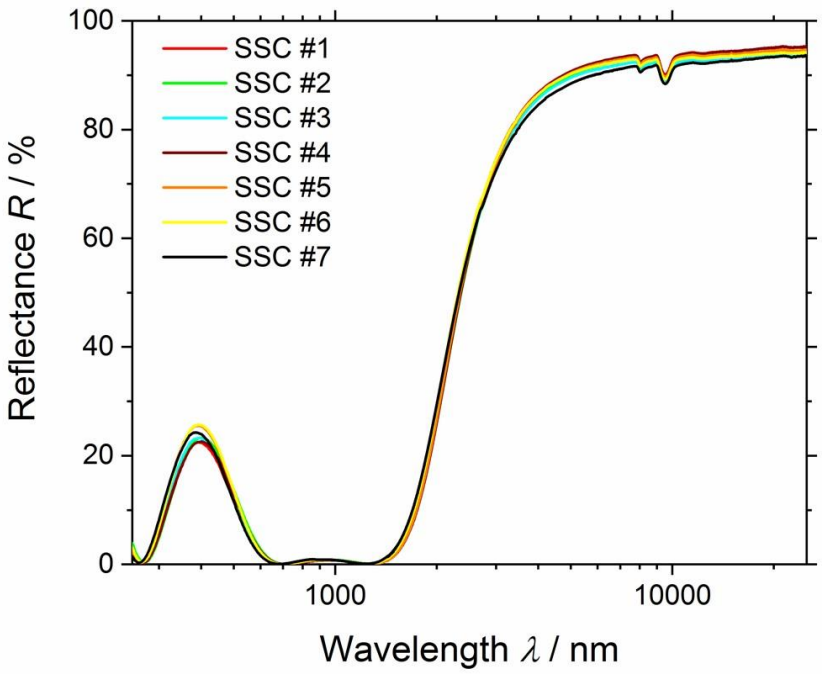

SI – 1: UV-vis-IR reflectance spectra of seven W/WAlSiN/SiON/SiO_2 SSC stack samples prior to the heating – cooling cycles to demonstrate sample reproducibility.